

SWIFT Code Assessment for Two Similar Transonic Compressors

R. V. Chima*

NASA Glenn Research Center, Cleveland, OH 44135

I. Abstract

One goal of the NASA Fundamental Aeronautics Program is the assessment of computational fluid dynamic (CFD) codes used for the design and analysis of many aerospace systems. This paper describes the assessment of the SWIFT turbomachinery analysis code for two similar transonic compressors, NASA rotor 37 and stage 35. The two rotors have identical blade profiles on the front, transonic half of the blade but rotor 37 has more camber aft of the shock. Thus the two rotors have the same shock structure and choking flow but rotor 37 produces a higher pressure ratio. The two compressors and experimental data are described here briefly. Rotor 37 was also used for test cases organized by ASME, IGTI, and AGARD in 1994-1998. Most of the participating codes over predicted pressure and temperature ratios, and failed to predict certain features of the downstream flowfield. Since then the AUSM⁺ upwind scheme and the $k-\omega$ turbulence model have been added to SWIFT. In this work the new capabilities were assessed for the two compressors. Comparisons were made with overall performance maps and spanwise profiles of several aerodynamic parameters. The results for rotor 37 were in much better agreement with the experimental data than the original blind test case results although there were still some discrepancies. The results for stage 35 were in very good agreement with the data. The results for rotor 37 were very sensitive to turbulence model parameters but the results for stage 35 were not. Comparison of the rotor solutions showed that the main difference between the two rotors was not blade camber as expected, but shock/boundary layer interaction on the casing.

II. Introduction

One goal of the NASA Fundamental Aeronautics Program is to assess computational fluid dynamic (CFD) codes now used by NASA and industry for the design and analysis of aircraft, spacecraft, propulsion systems, etc. The intent is to assess the current state of the art of these codes, then to periodically reassess the codes as advances are made in CFD. Five codes for turbomachinery problems fell under the Subsonic Fixed Wing Project. Developers and users of those codes met and chose two similar transonic compressors, NASA rotor 37 and stage 35, as test cases.

In 1978 Reid and Moore designed and tested four compressor stages, NASA stages 35-38, to investigate the effects of blade camber and aspect ratio on compressor performance¹⁻³. The tests were performed at NASA Glenn Research Center (formerly Lewis Research Center.) Stages 35 and 37 had low-aspect-ratio blades that gave the best performance. These blade rows have since been used for several CFD code assessment projects and were used for the present work.

Reid and Moore made aerodynamic surveys downstream of stage 35 and published the results in Ref. 2. This stage data is of interest for testing computational models for multistage turbomachinery including mixing plane models, the average passage model, and full unsteady blade row interaction models. Overall performance data for stage 37 was published in Ref. 1.

Rotor 37 was retested without the stator by Strazisar and Suder⁴⁻⁵ in the 1990's using both aerodynamic surveys and laser anemometry. Their data was used for a CFD blind test case conducted by ASME and IGTI in 1994 (unpublished,) and for a more detailed but non-blind test case conducted by AGARD⁶⁻⁷ in 1997-8.

Rotors 35 and 37 have design pressure ratios of 1.865 and 2.106, respectively. The front, transonic parts of the two blades are identical but rotor 35 has less camber on the aft part of the blade, does less diffusion, and thus produces a lower pressure rise. Thus, the ability of CFD codes to predict the different performance characteristics of the two similar compressors is of interest.

This report describes calculations of both rotor 37 and stage 35 made using the SWIFT code. SWIFT is a multiblock Navier-Stokes analysis code for turbomachinery developed by Chima⁹⁻¹³. For the original ASME and

* Aerospace Engineer, Inlets and Nozzles Branch, 21000 Brookpark Rd., MS 5-12, Associate Fellow AIAA

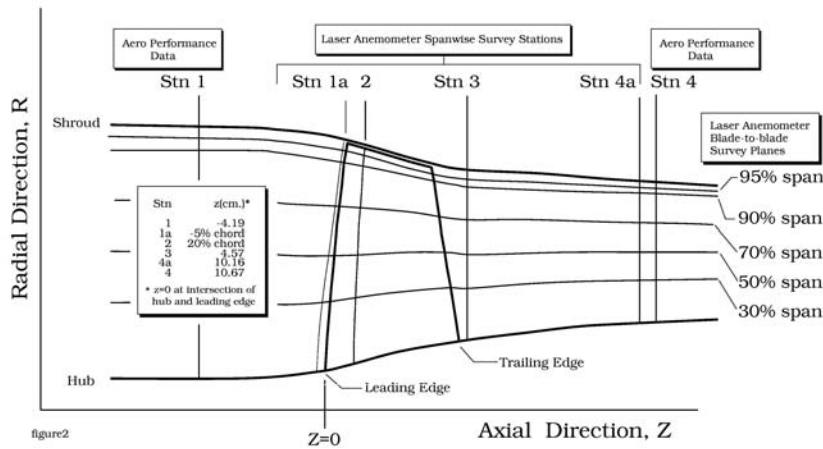


Figure 1. Rotor 37 flow path showing measurement stations.

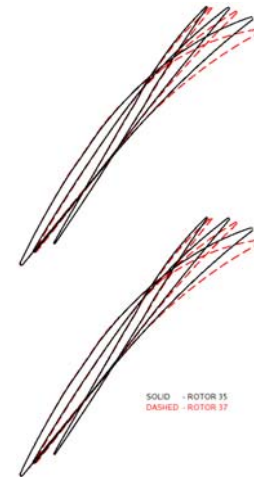


Figure 2. Blade profiles for rotor 37 (red, dashed) and rotor 35 (black, solid.)

AGARD rotor 37 test case⁶⁻⁷ SWIFT used a central-difference scheme and an algebraic turbulence model. For the present work it used the AUSM⁺ upwind differencing scheme^{8,9} and the latest version of the $k-\omega$ turbulence model¹⁴. A mixing plane model¹³ was used to analyze stage 35. Details of the experimental data and SWIFT code are described briefly. Detailed comparisons are made between the computed results and experimental data to show where the code agrees with data and where further work is needed. Finally the results for the two rotors are compared to determine why rotor 37 is harder to predict than rotor 35.

III. Test Cases

Rotor 37 is a low aspect ratio inlet rotor for a core compressor. It has 36 multiple circular-arc (MCA) blades and a design pressure ratio of 2.106 at a mass flow of 20.19 kg/sec. It was originally tested as a stage by Reid and Moore^{1,3}. The rotor was re-tested at NASA Glenn by Suder, et al.^{4,5} Radial distributions of static and total pressure, total temperature, and flow angle were measured at two axial stations located 4.19 cm upstream and 10.67 cm downstream of the blade hub leading edge, labeled stations 1 and 4 respectively in Fig. 1. Detailed laser anemometry measurements were made of the velocity field within the rotor and wake at several axial stations and on five spanwise planes also shown in Fig. 1. These measurements were used for a blind test case conducted by ASME and IGTI, and for a subsequent test case conducted by AGARD.

Stage 35 is an inlet stage for a core compressor, also designed and tested by Reid and Moore¹⁻³. Rotors 35 and 37 both have the same blade count, design speed, hub and casing radii, and tip clearance of about 0.2 percent span. Rotor 35 has the same blade profile as rotor 37 in the front, transonic half of the blade, so that the shock structure and choking flow of the two rotors are the same. However, rotor 37 has more camber than rotor 35 aft of the shock, giving a design pressure ratio of 2.106, while stage 35 has design pressure ratios of 1.865 for the rotor and 1.82 for the stage. Since rotor 37 has higher diffusion than rotor 35 it was expected to be a more difficult case for CFD codes to model. Profiles of the two rotor blades are shown at the hub, mid-span, and tip in Fig. 2.

Stator 35 has 46 MCA blades and is cantilevered from the casing with a clearance of ~0.5 percent span over a rotating hub. Radial distributions of static and total pressure, total temperature, and flow angle were measured downstream of the stator and averaged circumferentially, but no measurements were taken between the rotor and stator. Instead, rotor exit profiles were estimated by translating the mass-average total temperature and the mean of the three highest total pressures taken between the stators upstream along design streamlines. This introduces some uncertainty about the measurements behind the rotor.

In 1994 ASME and IGTI sponsored a blind test case for turbomachinery CFD codes at the 39th International Gas Turbine Conference held in The Hague, Netherlands (unpublished.) The same test case was later used by the AGARD Propulsion and Energetics Panel Working Group 26 as a CFD test case for examining the effects of grid and turbulence modeling on solution accuracy⁶⁻⁷. Sixteen different CFD codes were used to predict the performance

of rotor 37¹⁻³. One operating point at design speed and 98 percent of maximum flow was examined in detail. Three details of the measurements proved to be especially difficult to predict:

1. Most codes over predicted the overall pressure and temperature ratios and under predicted the efficiency. Predicted overall pressure ratios varied by nearly 10 percent and predicted efficiencies varied by about 6 points.
2. Most codes failed to predict the total pressure distribution downstream of the rotor below 40 percent span. The data shows a region of low total pressure that has been called a “pressure deficit.” This terminology implies that there is something wrong with the flow in that region and has prompted much discussion in the literature. Hah et al.¹⁵ suggested that the deficit is due to a corner stall on the rotor suction surface, while Shabbir, et al.¹⁶ showed evidence that it is due to air leaking into the flow path from the gap between the stationary and rotating parts of the hub at the rotor leading edge. Chima, et al.⁹ suggested that the low total pressure is an intrinsic feature of the rotor that tends to be smeared out by the central-difference schemes used by many CFD codes.
3. All codes over predicted the total temperature downstream of the rotor above 90 percent span by as much as 5.5 percent. The discrepancy was generally worse with algebraic turbulence models than with turbulent transport models. It was only mentioned briefly in the AGARD report, but it is either a fundamental problem with CFD methods for turbomachinery or an unrecognized error in the experimental results. In unpublished results provided after the ASME blind test case Strazisar and Suder calculated the total temperature close to the rotor trailing edge using laser measurements of tangential velocity and the Euler turbine equation. These temperatures were similar to the probe measurements further downstream, suggesting that the probe measurements are correct.

IV. SWIFT Code

The SWIFT code is a multi-block Navier-Stokes analysis code for turbomachinery blade rows. The code solves the Navier-Stokes equations on body-fitted grids using an explicit finite-difference scheme. The code includes viscous terms in the blade-to-blade and hub-to-tip directions, but neglects them in the streamwise direction using the thin-layer approximation. The discretized equations are solved with a multistage Runge-Kutta scheme using a spatially varying time step and implicit residual smoothing to accelerate convergence. The flow equations, discretization, and solution scheme were given in Ref. 10.

For the ASME and AGARD test cases SWIFT used a central-difference scheme and the Baldwin-Lomax turbulence model¹⁷. The same models were used to investigate the effects of tip clearance models in Ref. 12. In that work it was shown that a simple periodic boundary condition applied across the tip gap was as good as gridding the clearance gap for predicting overall performance. However, later work has shown that the gridded gap gives better predictions of spanwise profiles and has been used for all cases shown here. Ref. 12 also showed a computed separation on the casing of rotor 37 that proved to be important in the present work.

The Wilcox $k-\omega$ turbulence model¹⁴ was added to SWIFT in 1996. The numerical implementation was described for a two-dimensional case in Ref. 11. The $k-\omega$ model includes a transition model and roughness effects, and does not require calculation of distance from the wall. Recently SWIFT was updated to use Wilcox’s 2006 version of the $k-\omega$ model¹⁴. The newer model includes a cross diffusion term that reduces dependence on freestream values of ω , and a shear stress limiter that reduces the turbulent viscosity when production of turbulent kinetic energy exceeds the destruction. The shear stress limiter has been shown to improve results for shock separated flows¹⁴.

For multistage turbomachinery SWIFT uses a mixing plane approach with steady characteristic boundary conditions written in terms of perturbations about the mean flow from the neighboring blade row¹³. This allows close spacing between the blade rows without forcing the flow to be axisymmetric. Using a mixed-out average for the mean flow insures conservation between the blade rows. This approach was used for the calculations of stage 35 presented here.

The AUSM⁺ upwind scheme⁸ was added to SWIFT in 2003⁹. Results for rotor 37 showed that the AUSM⁺ scheme predicted details of the exit profiles that were measured experimentally but were not generally predicted by central-difference codes used in the ASME/AGARD test cases. The results suggest that the artificial dissipation used in central-difference schemes tend to smear out these details on relatively coarse spanwise grids, but that upwind schemes are able to capture them properly.

V. Computed Results

Computational grids used for the present calculations were generated using the TCGRID turbomachinery grid code developed by the author. C-type blade-to-blade grids were generated at a few spanwise locations using an elliptic grid generator developed by Sorenson¹⁸. The C-grids were reclustered spanwise using a hyperbolic tangent clustering function. Transfinite interpolation was used to generate an H-grid ahead of the blade, and algebraic

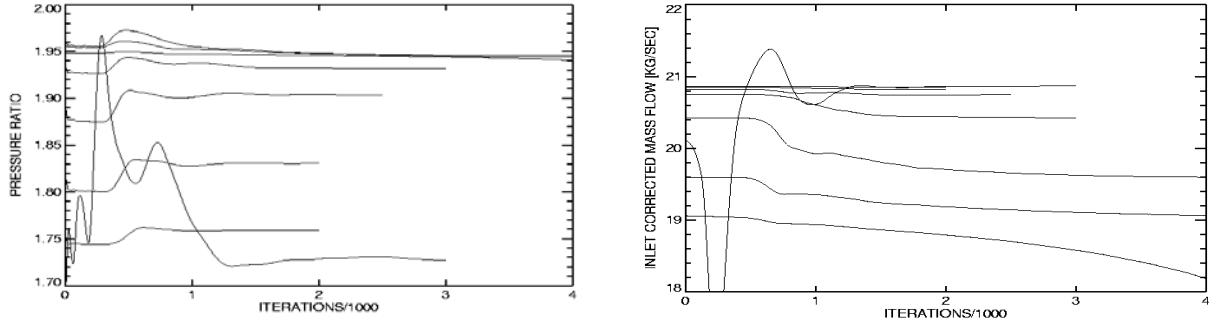


Figure 3. Convergence histories for stage 35. Pressure ratio (left) and inlet mass flow rate (right.)

methods were used to generate O-grids in hub and tip clearance regions. Grids for the rotor and stator of stage 35 were generated separately and merged later. Each grid overlapped its neighbor by one cell.

All SWIFT calculations were made using the AUSM⁺ upwind scheme and with several variations of the $k-\omega$ turbulence model discussed later. A four-stage Runge-Kutta scheme with a spatially-varying time step and implicit residual smoothing was used to converge the solution. Courant numbers were typically 5.6. Fig. 3 shows the convergence behavior of exit total pressure (left) and inlet mass flow (right) for eight operating points on a speed line for stage 35. The calculation at the highest mass flow (choked flow) was started from an initial guess and shows large variations in flow and pressure ratio that converge in 3,000 iterations. For this case the maximum residual converges linearly and drops 3 orders of magnitude. Calculations at lower flows were restarted from converged solutions at higher flow rates using a higher exit static pressure. In about 500 iterations the exit pressure disturbance reaches the inlet and the mass flow jumps to near its final value, then mass flow and pressure ratio converge gradually. The number of iterations for a fully converged solution increases near stall, and the calculations at the lowest mass flow are clearly diverging (stalled flow.)

A. Rotor 37

The grid for rotor 37 had three blocks as shown in Fig. 4. Grid sizes are given in Table 1. The blade-to-blade C-grid was optimized in a grid refinement study performed for the ASME/IGTI blind test case (unpublished.) The grid spacing at the blade and endwalls was 4×10^{-4} cm, giving $y^+ = 2$ to 4 at the first grid point off the walls. An O-type grid was used in the tip clearance gap with 13 points across the gap of .04 cm. The tip clearance grid was shown previously in Ref 12. The total grid had 871,846 points, which is about 3 times finer than the grids recommended by Dunham, et al.⁶

Table 1. Grid parameters for rotor 37.

Region	Type	Points (x, θ, r)	Total points
upstream	H	45 x 35 x 63	99,225
rotor	C	255 x 46 x 63	738,990
rotor tip	O	199 x 13 x 13	33,631
Total			871,846

Calculations for rotor 37 near choke took about 1.5 hours for 2,000 iterations on a PC with 2 Intel Xeon CPUs operating at 3.86 GHz. Calculations near stall took twice as long.

Figure 5 shows computed contours of static pressure at the mid span of rotor 37 at an operating point near stall. A strong, detached bow shock stands in front of the rotor.

The 100 percent speed line was calculated for rotor 37 using the AUSM⁺ upwind scheme and four variations of the $k-\omega$ turbulence model. The four variations included cases with and without transition and cases with and without the shear stress limiter. Fig. 6 shows comparisons of measured and computed characteristics of pressure ratio, temperature ratio, and adiabatic efficiency versus corrected mass flow computed with the four options. Results computed for the ASME blind test case using a central-difference scheme and the Baldwin-Lomax turbulence model are also shown. The ASME results were computed with a similar grid to the one used here.

The turbulence model had a very large effect on computed pressure ratios and a small effect on choking mass flow, as shown at the bottom of Fig. 6. The transition model predicted the highest pressure ratios, and the shear

stress limiter reduced the predicted pressure ratio for a given model. The Baldwin-Lomax model with the central-difference scheme gave pressure ratios close to the fully turbulent $k-\omega$ results without the stress limiter. The fully turbulent calculations with the shear stress limiter gave the best comparison to the experimental data, with the predicted pressure ratios completely within the experimental error bars $\Delta P_0 / P_0 = \pm 0.017$. The stall point computed for this case was 19.27 kg/sec, which is in excellent agreement with the measured stall point of 19.24 kg/sec. The stall point was not determined for the transition models.

Inlet boundary layers were specified as fully turbulent on the hub and casing. Nominal velocity profiles were calculated assuming turbulent wall/wake behavior and total pressure profiles were specified assuming constant static pressure. Analytic profiles of turbulence parameters k and ω were also specified. Thus the endwall boundary layers started and remained fully turbulent, and the effects of the transition model were limited to the blade surfaces. Using the transition model the pressure side of the blade was turbulent from the leading edge but the suction side remained laminar to the passage shock. The boundary layers after the shock had lower turbulent viscosity and were thinner than the fully turbulent cases. With lower blockage the transitional cases passed more flow and produced higher pressure ratios than the fully turbulent cases. Similar behavior has been seen both experimentally and computationally for rotor 37⁵.

Computed temperature ratios (Fig. 6, center) were all somewhat high, with the fully turbulent model with the shear stress limiter giving the best comparison to the experimental data. Here the experimental error bars are about the size of the points on the plot ($\Delta T_0 / T_0 = \pm 0.0022$), and none of the models is within this range. Computed efficiencies (top) tended to be low, with the transition models and Baldwin-Lomax model coming closest to the experimental data.

Figures 7-9 compare measured and computed spanwise profiles of total pressure, total temperature, and adiabatic efficiency 10 cm downstream of rotor 37 (station 4 in Fig. 1.). Results are shown at two operating points, a point near peak efficiency at a flow rate of 20.51 kg/sec, and a point near stall at 19.36 kg/sec. Computed results are shown for the fully turbulent model with the shear stress limiter that gave the best predicted pressure ratios. All computed results were averaged using a mixed-out averaging scheme that tends to give conservative estimates of overall total pressure. However the flow is nearly mixed out this far from the rotor and the averaging scheme has negligible effect on the results.

In Fig. 7 computed total pressure profiles agree fairly closely with the data except in the region of low total pressure below 40 percent span. Other researchers have suggested that this region is due to a corner stall¹⁵ or to hub leakage¹⁶. Previous work with SWIFT showed that both the central-difference and H-CUSP upwind differencing schemes smeared out the total pressure distribution in this region⁹. The AUSM⁺ upwind scheme used in the present results comes close to predicting this flow feature without modeling hub leakage.

Predicted total temperature profiles in Fig. 8 are in good agreement with the experimental data below 80 percent span. However, predicted temperature ratios near the casing are much higher than measured, with an error of about 5-8 percent of the overall temperature ratio. Similar discrepancies were seen in virtually every computed result in the AGARD test case⁷.

Several numerical experiments were carried out to try to reduce the total temperature discrepancy near the casing. The following results were noted:

1. Large increases in grid resolution made separately in the spanwise, blade-to-blade, and streamwise directions did not reduce the total temperature discrepancy.
2. Doubling the number of points across the clearance gap (from 13 to 25) decreased the discrepancy to 4-6 percent.
3. Reducing the tip clearance gap by half had minimal effect on the temperature profile. Surprisingly, completely eliminating the clearance gap only reduced the discrepancy by about half.
4. Replacing the adiabatic wall boundary condition at the casing with a low specified temperature reduced the total temperature very close to the wall but left most of the profile unchanged.
5. Inlet boundary layer thickness and freestream turbulence parameters had negligible effect on the total temperature profile.

Predicted efficiency profiles in Fig. 9 are slightly high at the hub where predicted total pressures are higher than measured, and very low above 80 percent span, where predicted total temperatures are much higher than measured.

B. Stage 35

The grid for stage 35 had five blocks as shown in Fig. 10. Grid sizes are given in Table 2. The grid spacing at the blade and endwalls was the same as that used for rotor 37. An O-type grid was used in the tip clearance gap over the

rotor with 9 points across a gap of .04 cm. An O-type grid was also used in the hub clearance gap under the stator with 11 points across a gap of .0762 cm (.03 in.) The total grid had 1,136,382 points.

Table 2. Grid parameters for stage 35.

Region	Type	Points (x, θ, r)	Total points
upstream	H	45 x 30 x 63	85,050
rotor	C	191 x 42 x 63	505,386
rotor tip	O	167 x 13 x 9	19,539
stator	C	191 x 42 x 63	505,386
stator hub	O	147 x 13 x 11	21,021
Total			1,136,382

Calculations for stage 35 near choke took about 1.9 hours for 2,000 iterations. Calculations near stall took twice as long.

Figure 11 shows computed contours of static pressure at the mid span of stage 35. This figure can be compared with Fig. 5 for rotor 37 at the same operating point to see that the two rotors have identical shock structures. This is to be expected since the two rotors have identical inlet velocity triangles and identical blade shapes up to mid chord. The aft part of rotor 37 produces a higher pressure rise than rotor 35, which is discussed later with Fig. 19. Pressure contours are locally discontinuous at the mixing plane interface between the rotor and stator but circumferentially averaged pressures are continuous. The stator has a normal shock on the suction surface at about 15 percent chord along most of the span. Recall that experimental measurements were taken downstream of the stators and that rotor performance was estimated as the average of the three highest total pressures between the stators. This assumes lossless flow between the stator blades so the presence of normal shocks in the stator could cause the rotor pressure ratio to appear low.

Fig. 12 shows comparisons of measured and computed speed lines of pressure ratio, temperature ratio, and adiabatic efficiency for the stage. Note that the data report² for stage 35 gives the stall point as 18.2 kg/sec, which is well off the plot to the left. It has been omitted from Fig. 12 in order to make the axes consistent with Fig. 6 for rotor 37. In a private communication Dr. Lonnie Reid, an author of Ref. 2, suggested that the rotor was probably in stable rotating stall at that operating point. The computed stall point for stage 35 was 19.42 kg/sec, which is similar to the stall point for rotor 37.

The computed results are in excellent agreement with the experimental data for all quantities, confirming the conjecture that rotor 35 might be easier to compute than rotor 37. The speed line shown in Fig. 12 used the AUSM⁺ scheme and the $k-\omega$ turbulence model with the fully turbulent and stress limiter options. Results computed using the other turbulence model options are shown for one back pressure. In this case the transition model had a negligible effect on the predicted performance but the stress limiter reduced the computed flow rate significantly. This result will be discussed later with Fig. 20.

Spanwise distributions of total pressure, total temperature, and adiabatic efficiency downstream of the rotor are compared to experimental data in Figs. 13–15. Two operating points are shown: a point near choke at 20.82 kg/sec (reading 3978 in Ref. 2) and a point near stall at 19.54 kg/sec (reading 3975 in Ref. 2.) Again, there is some uncertainty in the rotor exit profiles.

Computed total pressure profiles shown in Fig. 13 agree fairly well with the data above 40 percent span. Computed results near choke are in somewhat better agreement with the data than results near stall. Like rotor 37, rotor 35 has a region of lower total pressure below 40 percent span that is not quite captured by the calculations.

Computed total temperature profiles shown in Fig. 14 agree well with the measurements except above 90 percent span, where the predicted total temperature is 21–28 C greater than the measured value. Although the temperature discrepancy at the wall is greater here than for rotor 37, the discrepancy starts much closer to the wall where there is less flow, so that the overall total temperature ratio in Fig. 12 is still in excellent agreement with the data. Similarly, computed efficiency profiles shown in Fig. 15 are in fairly good agreement with the data below 90 percent span, so that the overall efficiency prediction in Fig. 12 is excellent.

Spanwise distributions of axial velocity, loss coefficient, and flow angle downstream of the stator are shown in Figs. 16–18. Computed axial velocity profiles shown in Fig. 16 are slightly high for the operating point near choke but in excellent agreement with the data near stall. The computed profiles show a large velocity deficit below 10 percent span that is not seen in the data. This deficit is due to the hub clearance flow (see Fig. 20) and could be due to incorrect gap size, insufficient grid resolution, or turbulence modeling.

Computed stator loss coefficient profiles shown in Fig. 17 are in excellent agreement with the data at choke but slightly low near stall. The loss coefficient is given by

$$\omega = \frac{P_{01} - P_{02}}{P_{01} - P_1} \quad (1)$$

Computed exit flow angles shown in Fig. 18 show the correct trends with span but are about 4–5 degrees low everywhere. It seems unlikely that this large of a discrepancy could be due to errors in the computed stator boundary layer. Angles were measured experimentally using self-nulling wedge probes with an uncertainty of $\pm 1.0^\circ$. It is not clear whether the angles were averaged directly or if they were converted to velocity components that were averaged first and then used to compute an angle, so this is a possible reason for the discrepancy. It is also possible that the measurements include the unsteady effects of the passing rotor wakes that are not captured by the mixing plane analysis used here.

C. Comparison of Rotor 37 and Stage 35

It is instructive to compare the solutions for rotor 37 and stage 35 to see what features of the flow fields make rotor 37 so much more sensitive to turbulence model parameters than rotor 35. The front, transonic halves of the two rotors are identical and comparison of the static pressure contour plots for a case near stall in Figs. 5 and 11 show that the shocks are identical at mid span.

Since rotor 37 has more aft camber than rotor 35 it was suspected that suction side shock/boundary layer interaction could be much more important in rotor 37. Fig. 19 compares the surface static pressure distributions on the two rotors at mid span at a point near stall and shows that this is not the case. In fact the two rotors have identical pressure distributions over the entire suction side, with the additional loading on rotor 37 occurring entirely on the pressure side where the boundary layer is thin and well-behaved. This was seen to be true along most of the span.

Fig. 20 compares entropy contours at mid pitch for rotor 37 (top) and stage 35 (bottom.) Entropy rise is independent of frame of reference and shows the development of loss through the blade rows. It is given by

$$\frac{ds}{R} = \ln \left(TR \times PR^{\frac{1-\gamma}{\gamma}} \right) \quad (2)$$

where TR is the temperature ratio and PR is the pressure ratio. The plots show that the inlet boundary layers, bow shocks, and passage shocks are identical along the span for the two rotors. The biggest difference between the two rotors occurs at the casing where the passage shock and clearance vortex meet and cause the casing boundary layer to separate with a classic lambda shock structure. The additional diffusion in rotor 37 creates a much larger separation than in rotor 35, and it is this separation that is so sensitive to turbulence model effects. In particular the shear stress limiter is designed to decrease the turbulent viscosity in exactly this type of flow, and it gave the best overall performance results for rotor 37.

The stage 35 calculations in Fig. 20 show a slight discontinuity in entropy across the mixing plane. The average solution, however, is continuous. This figure also shows a high loss region where the hub clearance flow under the stator intersects the mid pitch display plane. When averaged circumferentially the loss in this region is responsible for the deficit in axial velocity near the hub noted in Fig. 16.

Spanwise distributions of overall entropy rise for the two rotors are compared with experimental data in Fig. 21. The agreement is excellent over most of the lower span. Surprisingly, near the hub rotor 35 produces a slightly larger entropy rise than rotor 37, as seen in both the computations and the data. Between 20 and 80 percent span the two rotors produce nearly identical entropy rises, indicating that the additional camber in rotor 37 does not contribute to additional profile loss. Entropy rise is nearly linear with span up to about 80 percent span for rotor 37 and to about 90 percent span for rotor 35. Above those locations the rate of entropy rise with span increases sharply, more so for rotor 37 than rotor 35. The calculated entropy rise is greater than the measured entropy rise for both rotors, consistent with the high predicted total temperatures shown in Figs. 8 and 14.

V. Summary and Conclusions

The SWIFT turbomachinery analysis code was used to predict the performance of two transonic compressors, NASA rotor 37 and stage 35. Relatively fine computational grids were used with 0.9 – 1.3 million points and 8 – 12

cells across clearance gaps. The AUSM⁺ upwind scheme and the Wilcox 2006 k- ω turbulence model were used for all cases.

Several variations of the turbulence model were run and shown to have a large effect on the predicted pressure ratio for rotor 37. Calculations using the transition model remained laminar up to the shock on the suction side of the blade and overestimated the pressure ratio. Fully turbulent calculations using the stress limiter gave excellent agreement with measured pressure ratios. Turbulence model options had a much smaller effect on stage 35.

Spanwise profiles of circumferentially averaged flow properties downstream of the blade rows were compared to experimental data. In general the agreement was very good, certainly much better than the agreement obtained for the ASME blind test case in 1994 using a central difference scheme and the Baldwin-Lomax turbulence model.

Three areas where the code did not agree with the data were noted:

Hub total pressure deficit. Predicted exit total pressures below 40 percent span did not quite match the so-called deficit seen in the data. Use of the AUSM⁺ upwind scheme has greatly improved the prediction of the deficit, but there is still a small discrepancy. This feature of the flow field seems to be intrinsic to the rotor design but could still be related to hub leakage in the experiment, as suggested by Shabbir, et al.

Over prediction of total temperature near the casing. Predicted exit total temperatures were high near the casing. This discrepancy was also seen in all of the results published in the AGARD test case report. Probe measurements of total temperature were consistent with temperatures computed from laser anemometry data, so the data seems to be correct. The discrepancy was reduced somewhat by doubling the grid across the clearance gap but was not greatly affected by other grid refinement, the clearance size, or turbulence model parameters.

Under prediction of exit flow angles for stator 35. The predicted exit flow angles for stator 35 were several degrees lower than the data. This could be due to differences in the way that the experimental angles were averaged or to unsteady effects not captured by the mixing plane analysis.

Rotors 35 and 37 have identical blade profiles on the front, transonic part of the blades but rotor 37 has more camber on the aft part of the blade, so the solutions for the two rotors were compared to see why turbulence model parameters had a much larger effect on rotor 37. The two rotors had identical shock systems as expected, but surprisingly the pressure distributions were identical along the entire suction side, not just up to the shock. All the additional loading on rotor 37 occurred on the pressure surface where the boundary layers are thin and well behaved.

The key difference between the two rotors occurred on the casing where the passage shock and clearance vortex meet and cause the casing boundary layer to separate. The additional aft camber in rotor 37 increases the adverse pressure gradient and the strength of the clearance flow, both of which would make the separation larger. The separation was sensitive to turbulence model parameters and seemed to be modeled best by assuming fully turbulent flow and using a stress limiter. However, the predicted separation is probably still too large, as seen indirectly in the over prediction of total temperature and entropy rise far downstream.

The fact that all codes in the AGARD test case over predicted total temperature near the casing suggests that no codes do well for the shock/vortex/boundary layer interaction there. Unfortunately there is no good experimental data in this region - existing probe and laser data both stop just below the separated region at about 95 percent span. Additional measurements in the separated region would be extremely useful for finally explaining these rotors, for improving CFD codes for highly loaded blades, and ultimately for designing rotors with better performance near the casing.

References

- ¹Reid, L. and Moore, R. D., "Design and Overall Performance of Four Highly-Loaded, High Speed Inlet Stages for an Advanced, High Pressure Ratio Core Compressor," NASA TP-1337, 1978.
- ²Reid, L. and Moore, R. D., "Performance of a Single-Stage Axial-Flow Transonic Compressor with Rotor and Stator Aspect Ratios of 1.19 and 1.26, Respectively, and with Design Pressure Ratio of 1.82, NASA TP-1338, 1978.
- ³Reid, L. and Moore, R. D., "Experimental Study of Low Aspect Ratio Compressor Blading," ASME Paper 80-GT-6, Mar. 1980.
- ⁴Suder, K. L., and Celestina, M. L., "Experimental and Computational Investigation of the Tip Clearance Flow in a Transonic Axial Compressor Rotor," NASA TM-106711, 1994.
- ⁵Suder, K. L., Chima, R. V., Strazisar, A. J., and Roberts, W. B., "The Effect of Adding Roughness and Thickness to a Transonic Axial Compressor Rotor," ASME *J. Turbomachinery*, Vol. 117, Oct. 1995, pp. 491-505.
- ⁶Dunham, J. ed. "CFD Validation for Propulsion System Components," AGARD Advisory Report 355, AGARD, Neuilly-Sur-Seine, France, May, 1998.
- ⁷Dunham, J. and Meauzé, G., "An AGARD Working Group Study of 3-D Navier-Stokes Codes Applied to Single Turbomachinery Blade Rows," ASME Paper 98-GT-50, June, 1998.
- ⁸Liou, M.-S. and Steffen, Jr., C. J., "A New Flux Splitting Scheme," *J. Computational Physics*, Vol. 107, No. 1, July 1993, pp. 23-39. Also NASA TM 104404, May 1991.

⁹Chima, R. V. and Liou, M.-S., "Comparison of the AUSM⁺ and H-CUSP Schemes for Turbomachinery Applications," AIAA Paper AIAA-2003-4120. Also NASA TM-2003-212457.

¹⁰Chima, R. V., "Viscous Three-Dimensional Calculations of Transonic Fan Performance," in *CFD Techniques for Propulsion Applications*, AGARD Conference Proceedings No. CP-510, AGARD, Neuilly-Sur-Seine, France, Feb. 1992, pp. 21-1 to 21-19. Also NASA TM-103800.

¹¹Chima, R. V., "A $k-\omega$ Turbulence Model for Quasi-Three-Dimensional Turbomachinery Flows," AIAA Paper 96-0248. Also NASA TM-107051.

¹²Chima, R. V., "Calculation of Tip Clearance Effects in a Transonic Compressor Rotor," ASME Paper 96-GT-114, June 1996. Also NASA TM-107216.

¹³Chima, R. V., "Calculation of Multistage Turbomachinery Using Steady Characteristic Boundary Conditions," AIAA Paper 98-0968, Jan. 1998. Also NASA TM-1998-2066.

¹⁴Wilcox, D. C., "Formulation of the $k-\omega$ Turbulence Model Revisited," AIAA Paper 2007-1408, Jan. 2007.

¹⁵Hah, C. and Loellbach, J., "Development of Hub Corner Stall and Its Influence on the Performance of Axial Compressor Blade Rows," ASME Paper 97-GT-42, June, 1997.

¹⁶Shabbir, A., Celestina, M. L., Adamczyk, J. J., and Strazisar, A. J., "The Effect of Hub Leakage Flow on Two High Speed Axial Compressor Rotors," ASME Paper 97-GT-346, June, 1997.

¹⁷Baldwin, B. S., and Lomax, H., "Thin-Layer Approximation and Algebraic Model for Separated Turbulent Flows," AIAA Paper 78-257, Jan. 1978.

¹⁸Sorenson, R. L., "A Computer Program to Generate Two-Dimensional Grids About Airfoils and Other Shapes by Use of Poisson's Equation," NASA TM-81198, 1980.

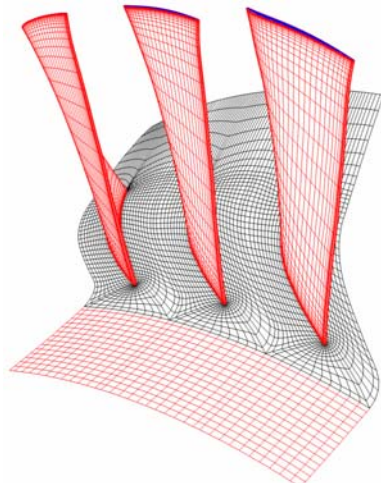


Figure 4. Computational grid for rotor 37.

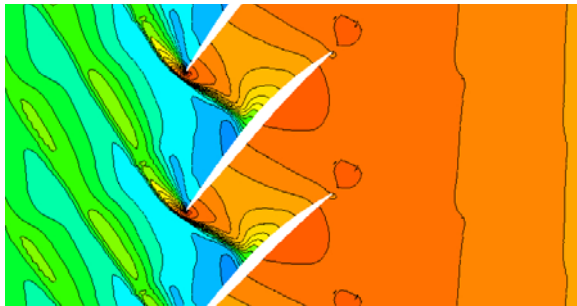


Figure 5. Static pressure contours for rotor 37 at mid span, near stall.

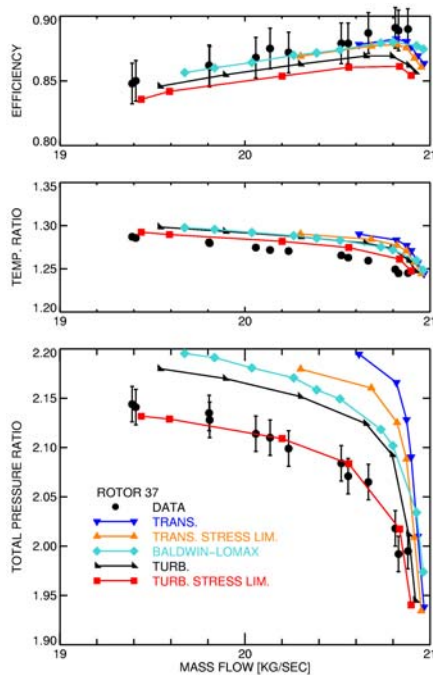


Figure 6. Measured and computed P_0 , T_0 , and η speed lines for rotor 37.

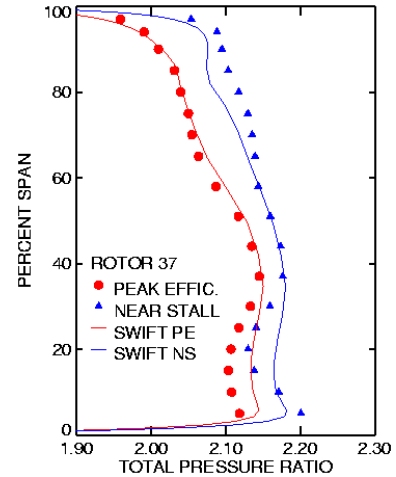


Figure 7. Measured and computed profiles of total pressure downstream of rotor 37.

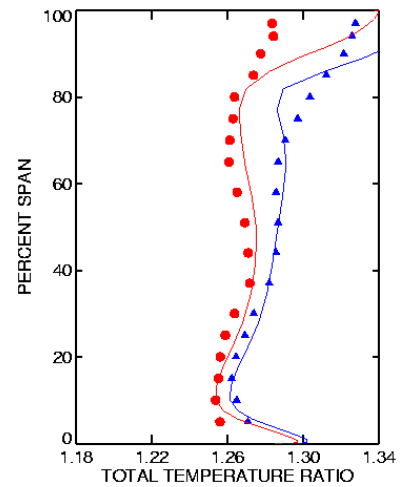


Figure 8. Measured and computed profiles of total temperature downstream of rotor 37.

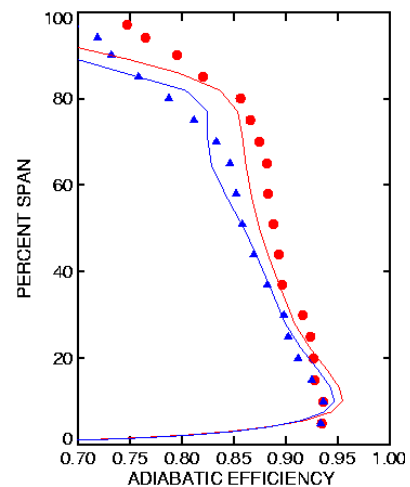


Figure 9. Measured and computed profiles of adiabatic efficiency downstream of rotor 37.

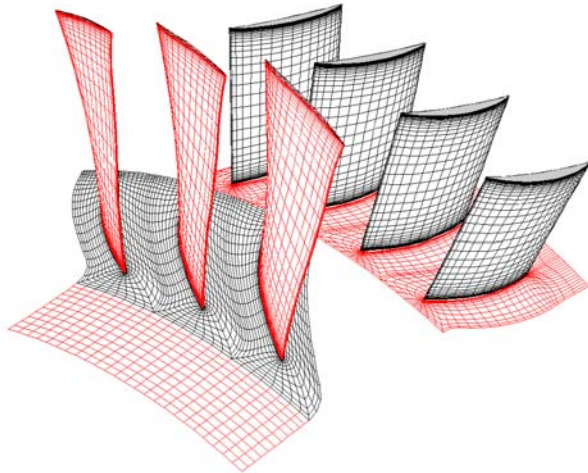


Figure 10. Computational grid for stage 35.

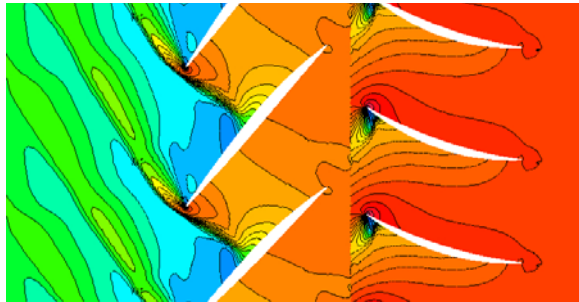


Figure 11. Static pressure contours for stage 35 at mid span, near stall.

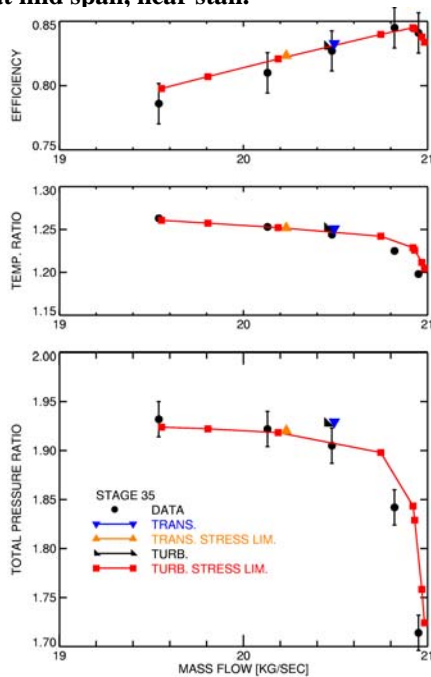


Figure 12. Measured and computed P_0 , T_0 , and η speed lines for stage 35. Measured stall point at 18.2 kg/sec not shown.

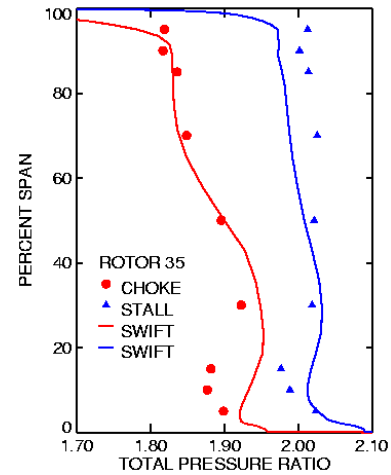


Figure 13. Measured and computed profiles of total pressure downstream of rotor 35.

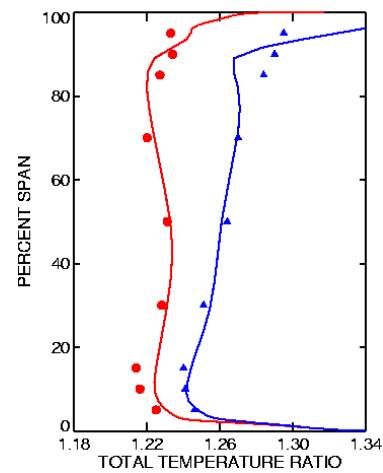


Figure 14. Measured and computed profiles of total temperature downstream of rotor 35.

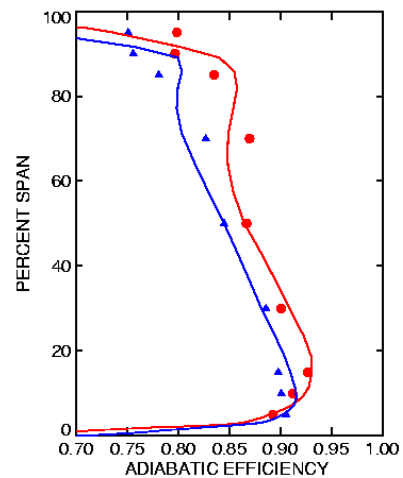


Figure 15. Measured and computed profiles of adiabatic efficiency downstream of rotor 35.

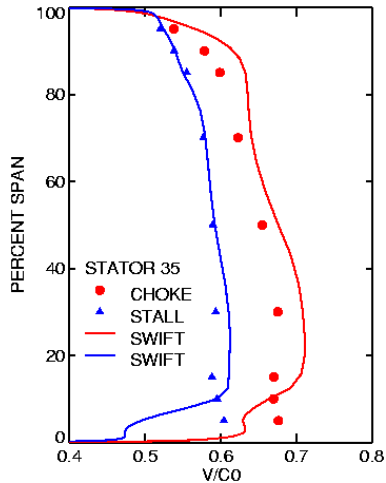


Figure 16. Measured and computed profiles of axial velocity downstream of stator 35.

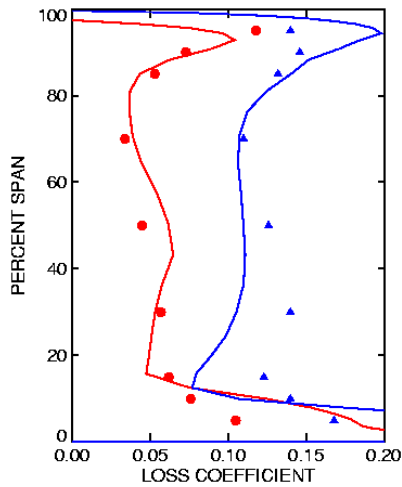


Figure 17. Measured and computed profiles of loss coefficient downstream of stator 35.

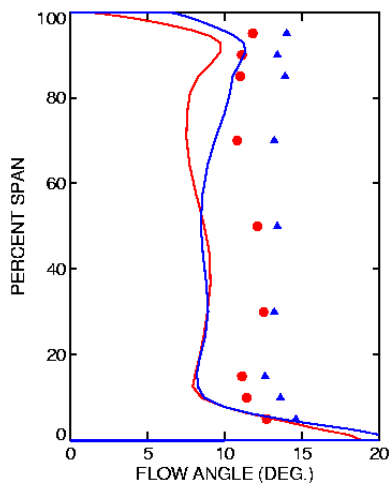


Figure 18. Measured and computed profiles of flow angle downstream of stator 35.

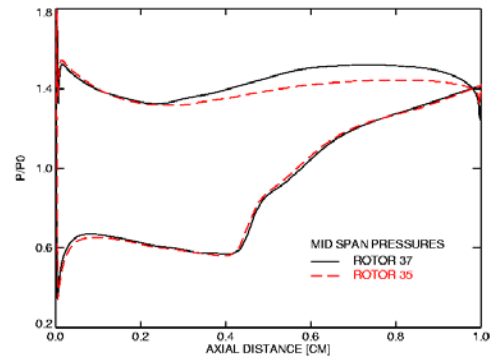


Figure 19. Comparison of static pressure distributions on rotors 35 and 37 at mid span.

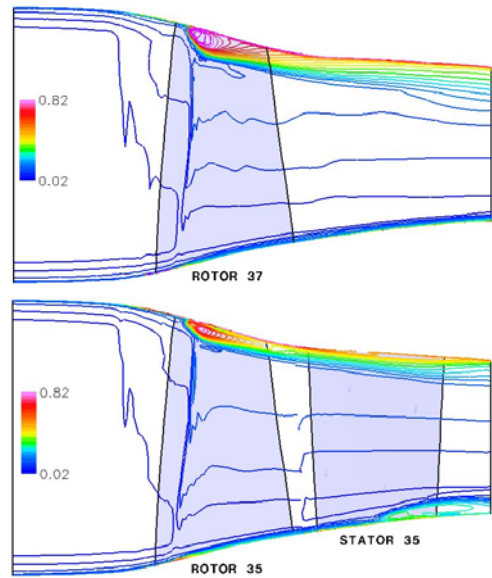


Figure 20. Comparison of entropy contours in rotor 37 and stage 35 at mid pitch.

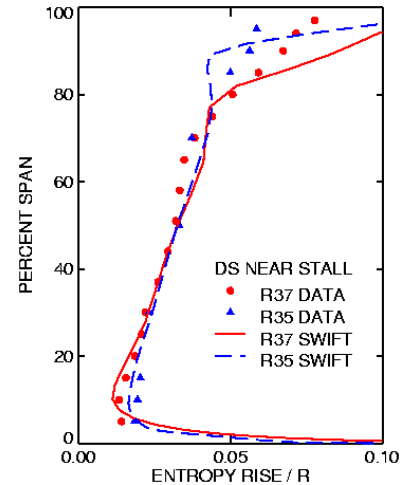


Figure 21. Measured and computed profiles of entropy downstream of rotors 35 and 37.